Novel Preparation Methods of 52Mn for ImmunoPET Imaging

Graves, Stephen A.; Hernandez, Reinier; Fonslet, Jesper; England, Christopher G.; Valdovinos, Hector F.; Ellison, Paul A.; Barnhart, Todd E.; Elema, Dennis Ringkjøbing; Theuer, Charles P.; Cai, Weibo; Nickles, Robert J.; Severin, Gregory

Published in:
Bioconjugate Chemistry

Link to article, DOI:
10.1021/acs.bioconjchem.5b00414

Publication date:
2015

Document Version
Peer reviewed version

Article

Novel Preparation Methods of Mn for ImmunoPET Imaging

Stephen A Graves, Reinier Hernandez, Jesper Fonslet, Christopher G England, Hector F Valdovinos, Paul A Ellison, Todd E. Barnhart, Dennis R Elema, Charles P Theuer, Weibo Cai, Robert J Nickles, and Gregory W Severin

Bioconjugate Chem., **Just Accepted Manuscript** • DOI: 10.1021/acs.bioconjchem.5b00414 • Publication Date (Web): 28 Aug 2015

Novel Preparation Methods of ^{52}Mn for ImmunoPET Imaging

Stephen A. Graves[1], Reinier Hernandez[1], Jesper Fonslet[2], Christopher G. England[1], Hector F. Valdovinos[1], Paul A. Ellison[1], Todd E. Barnhart[1], Dennis R. Elema[2], Charles P. Theuer[3],Weibo Cai[1,4,5], Robert J. Nickles[1] and Gregory W. Severin[2]*

[1]Univeristy of Wisconsin – Madison, Department of Medical Physics
[2]Technical University of Denmark, Center for Nuclear Technologies
[3] TRACON Pharmaceuticals, San Diego, CA 92122, United States
[4]University of Wisconsin – Madison, Department of Radiology
[5]University of Wisconsin – Madison, Carbone Cancer Center

*Corresponding author information:
Gregory W. Severin
gsev@dtu.dk
Frederiksborgvej 399 building 202, 4000 Roskilde, Denmark
Phone: +45 46 77 53 69

Abstract

^{52}Mn ($t_{1/2}$ =5.59 d, ß$^+$ = 29.6%, $E_{ßave}$ = 0.24 MeV) shows promise in positron emission tomography (PET) and in dual-modality manganese-enhanced magnetic resonance imaging (MEMRI) applications including neural tractography, stem cell tracking, and biological toxicity studies. The extension to bioconjugate application requires high specific activity ^{52}Mn in a state suitable for macromolecule labeling. To that end a ^{52}Mn production, purification, and labeling system is presented, and its applicability in preclinical, macromolecule PET is shown using the conjugate ^{52}Mn-DOTA-TRC105. ^{52}Mn is produced by 60 µA, 16 MeV proton irradiation of natural chromium metal pressed into a silver disc support. Radiochemical separation proceeds by strong anion exchange chromatography of the dissolved Cr target, employing a semi-organic mobile phase, 97:3 (v:v) ethanol: HCl (11M, aqueous). The method is 62 ± 14% efficient (n=7) in ^{52}Mn recovery, leading to a separation factor from Cr of (1.6 ± 1.0) x10^6 (n = 4), and an average effective specific activity of 0.8 GBq/µmol (n = 4) in titration against DOTA. ^{52}Mn-DOTA-TRC105 conjugation and labeling demonstrate the potential for chelation applications. *In vivo* images acquired using PET/CT in mice bearing 4T1 xenograft tumors are presented. Peak tumor uptake is 18.7 ± 2.7 %ID/g at 24 hours post injection and *ex vivo* ^{52}Mn biodistribution validates the *in vivo* PET data. Free $^{52}Mn^{2+}$ (as chloride or acetate) is used as a control in additional mice to evaluate the non-targeted biodistribution in the tumor model.

Keywords

Positron emission tomography (PET), immunoPET, manganese-52 (Mn-52, ^{52}Mn), CD105/Endoglin, Tumor angiogenesis, TRC105, molecular imaging, DOTA chelation, organic anion exchange, trace metal analysis (MP-AES, ICP-OES)

Introduction

Interest in ^{52}Mn[1]-based positron emission tomography (PET) applications has increased dramatically in recent years partly due to PET/MRI technological advancements and partly due to increased demand for long-lived PET radiometals such as ^{64}Cu and ^{89}Zr.[1, 2] For MRI, the T_1-shortening properties of bulk manganese are employed in manganese-enhanced magnetic resonance imaging (MEMRI). However, the biological toxicity of bulk manganese[3] has hampered the development and progression of otherwise useful applications such as diffusion-tensor neuronal fiber tractography[4-6], nociceptive activity detection[7], functional imaging of brain activation[8], diagnosis and staging of pancreatic cancer[9], heptocellular carcinoma detection[10], cell tracking[11, 12] and evaluation of cardiac inotropic therapy[13]. Manganese-52-based PET tracer

[1] Throughout the text ^{52}Mn refers to the ground state nuclide, ^{52g}Mn, rather than the short-lived isomer ^{52m}Mn.

alternatives may provide analogous data with lower toxicity and thereby promote clinical application.

Additionally ^{52}Mn may offer advantages over traditional ^{64}Cu or ^{89}Zr immunoPET in situations where treatment response monitoring at late time-points (2-3 weeks) is desired. In cases where radioimmunotherapy is initiated with long-lived nuclides such as ^{177}Lu, the full time-course of treatment could be monitored by ^{52}Mn PET. Further, due to the abundance of coincident high energy gammas, ^{52}Mn is one of relatively few nuclides that can be used in third-gamma coincidence PET for either event dual nuclide event tagging or combined Compton telescope PET tomography[14]. Despite this, clinical translation should proceed with caution due to the preponderance of coincident high energy gammas: 744 keV (90%), 935 keV (95%) and 1434 keV (100%). Coupled with the myriad biological roles of manganese, which may lead to prolonged retention of radiomanganese in critical organs, careful dosimetry prior to translation should be considered.

A common method for high-yield production of ^{52}Mn is via the ^{52}Cr(p,n) reaction: a route available using small biomedical cyclotrons[15-18]. Due to the natural 83.8% abundance of ^{52}Cr in ^{nat}Cr and the low propensity for impurity formation of other Mn isotopes during proton irradiation, ^{nat}Cr, which is available in high purity from various distributors, is an inexpensive alternative to enriched target material. The main radionuclidic impurity formed from the irradiation of ^{nat}Cr is ^{54}Mn ($t_{1/2}$ = 312 d) with an energy dependent co-production rate, representing 0.1-0.4% of the ^{52}Mn activity at the end of a short bombardment at 16 MeV[16, 19]. For one hour 16 MeV irradiations on a thick Cr target, the expected yield of ^{52}Mn is approximately 9.5 MBq/μA[19].

In order to separate ^{52}Mn from the bulk Cr matrix, anion exchange from semi-aqueous hydrochloric acid media is a simple trap-and release technique. Previously published methods for separating manganese from chromium involving anion exchange rely upon the formation of anionic chloride complexes of manganese[17, 18, 20]. Notably, there is a marked enhancement in the formation of the anionic manganese chlorides when hydration is limited by using non-aqueous solvents[21]. However, under similar conditions Cr^{3+} does not form anionic chloride complexes. This behavior is evident in the distribution coefficients for Mn and Cr against anion exchange resin from 97% EtOH 0.3M HCl solutions[21], where the resin affinities are sufficiently disparate for trap-and-release purification of ^{52}Mn from bulk Cr with small resin beds.

As a first test for bifunctional chelation of Mn to macromolecules, the common chelate DOTA (1,4,7,10 tetraazacyclododecane 1,4,7,10 tetraacetic acid) is an obvious choice due to its ubiquity in radiochemical applications and the reported stability of DOTA chelates with Mn(II)[22]. Because the long physical half-life of ^{52}Mn ($t_{1/2}$ = 5.591 days[23]) lends itself well to the long biological circulation times in radioimmunoPET applications, a demonstration of the stable chelation of ^{52}Mn using bifunctionalized DOTA conjugated to a monoclonal antibody proves its usefulness as a radiotracer. For this study TRC105, a chimeric human/murine immunoglobulin G (IgG_1) monoclonal antibody (mAb) which binds to the angiogenic marker CD105 with very high specificity, was chosen as the model compound due to the extensive body of data available that describes its biodistribution with other radiometals and chelates[24-26]. This antibody is currently associated with seventeen phase I and II multi-center clinical trials which are planned, underway, or already completed investigating the therapeutic efficacy in a variety of solid tumors either alone or as an adjunct to other treatment techniques.

The purpose of this report is to describe a methodology for the production and purification of ^{52}Mn that is amenable to bioconjugate chemistry. A simple cyclotron target made of chromium metal is described, and the procedure for extracting ^{52}Mn from the Cr matrix is given. The chemical purity of the produced ^{52}Mn is demonstrated by trace metal analysis and chelation with DOTA. Finally, the suitability of DOTA as a bifunctional chelate for Mn is investigated by in-vivo experiments of ^{52}Mn-DOTA-TRC105 in 4T1 xenograft-bearing mice, and comparison with the biodistribution of weakly coordinated $^{52}Mn^{2+}$. To our knowledge, the formation of ^{52}Mn-DOTA-TRC105 constitutes the first bioconjugate radiomanganese PET agent, and acts as a benchmark of the purity of ^{52}Mn required for targeted PET.

Results and Discussion

Target Fabrication, Irradiation, Dissolution and Column Separation

The goal of creating a simple design for metal chromium irradiation was met by pressing high purity chromium with a hydraulic press into a silver backing at 30kN. The Cr/Ag pressed targets were remarkably resilient, withstanding 60 µA of 16 MeV protons for two hours without failure. An example target is shown in Figure 1. Based on the alloying behavior of chromium and silver[27], we speculate that in addition to any mechanic bonding, 30 kN may be sufficient to form an eutectic alloy at the boundary between the two metals facilitating thermal conduction and physical stability. The average end-of-bombardment ^{52}Mn yield was 5 ± 1 MBq/µAh (n=12), which is approximately half of our previously measured thick target production rate of 9.5±1 MBq/µAh[19] due to target thickness irregularities and partial beam-spot coverage.

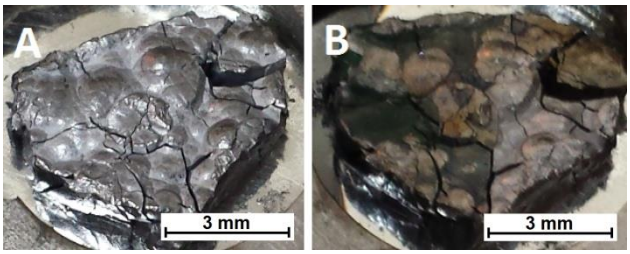

Figure 1: 99.999% pure chromium pellet imbedded in silver, direct-jet watercooled on the rear target face, before (A) and after (B) irradiation by 60 µA of 16 MeV protons for one hour.

Following irradiation, targets were etched with HCl and the resulting solution was diluted with ethanol. This was done in order to reach a condition where dissolved Mn(II) anionic chloride complexes extract onto strong anion-exchange resin while hydrated Cr^{3+} passes through. Upon switching to a fully aqueous 6M HCl solution ^{52}Mn was released from the resin bed. The entire procedure of trap-and-release, alternating from ethanolic to aqueous mixtures was repeated three times on three separate small AG-1x8 columns.

^{52}Mn extraction from ethanolic HCl onto AG-1x8 was 73 ± 13%, 91 ± 4%, and 92 ± 5% efficient (n=7) at each of the column passes. The low first-step separation efficiency is likely due to the low HCl and ethanol concentrations for loading, approximately 0.11 M and 95% respectively, compared to the ideal concentrations of >0.3 M HCl and >97% ethanol. It is likely that ^{52}Mn trapping could be greatly improved by drying the dissolved target material before reconstituting in 0.3 M HCl, 97% EtOH. Alternatively, a hydrogen chloride ethanol or dioxane solution (4.0 M HCl in dioxane, Sigma Aldrich Inc.) could be used after target dissolution to obtain the desired HCl concentration without the burden of added aqueous volume. The overall ^{52}Mn recovery efficiency of 62 ± 14% (n=7) was sufficient for our purposes, as it was nearly twice as efficient as the previously reported trioctylamine based extraction approach to ^{52}Mn/^{nat}Cr separation[19] and more easily lends itself to automation.

Chromium content in the eluted fractions fell successively at each step by factors of 601 ± 31, 80 ± 6, and 42 ± 5 (n=1), as seen in Table 1. The overall chromium separation factor was $1.6x10^6$ ± $1.0x10^6$ (n = 4) as measured by trace metal analysis. During the first column separation, the resin became uniformly green-tinted indicating a slight retention of Cr^{3+}. This chromium did not wash off of the resin in any appreciable way with repeated rinses of the ethanolic HCl. However upon elution of ^{52}Mn, this species of Cr also co-eluted to a small degree. Similar effects were observed in the other two subsequent column separations by tracing the Cr content with microwave plasma atomic emission spectrometry (MP-AES). Surprisingly this behavior contrasts with the published distribution coefficients of Pietrzyk et al., in that the extracted species of Cr was not behaving chromatographically[21]. This is ultimately the reason why three sequential separations were required to achieve the necessary purity for labeling, rather than repeated washings. The act of removing the Cr from the column and then re-constituting it in the ethanolic solutions appeared to reset the Cr form dichotomy, although with diminishing returns. This is likely due to the formation of different hydration states of Cr^{3+} in solution and their slow interchange[28]. Regardless, the two additional column repetitions were not restrictive to rapid isolation of the product ^{52}Mn.

Table 1. Stepwise chromium reduction in a single production batch quantified by MP-AES hold-back measurements.

	Cr Mass (µg)	Step Separation Factor	Cumulative Separation Factor
Dissolved Target	(4.05 ± 0.04) $x10^3$	-	-

After Column #1	360 ± 18	601 ± 31	(6.0±0.3) x10^2
After Column #2	3.82 ± 0.19	80 ± 6	(4.8 ± 0.4) x10^4
After Column #3	0.083 ± 0.008	42 ± 5	(2.0 ± 0.3) x10^6

Analysis of Purity: Chelation and Trace Metal Quantification

Titration of the ^{52}Mn sample against varying concentrations of DOTA resulted in an effective specific activity of up to 2GBq/µmol. MP-AES trace metal analysis of the final samples are given in Table 2. If all transition metal impurities are considered to be competitive for DOTA chelation, reactions at a level of about 4GBq/µmol are predicted from the data. It is probable that a significant portion of the trace metal impurities come from the large volumes of ethanol involved in the separation process. For example, we observed iron in the ethanol stock at a concentration of 31 ng/mL, or roughly 5 µg total iron mass in a typical production. An additional in-house distillation of commercial ethanol might be effective in producing metal-free ethanol, reducing impurities in future ^{52}Mn productions.

Table 2: Trace metal analysis by microwave plasma atomic emission spectrometry of the radiochemically separated ^{52}Mn product from approximately 400 mg dissolved Cr target material in three independent separations (Runs 1-3).

Element	Run 1 Mass (µg)	Run 2 Mass (µg)	Run 3 Mass (µg)
Cr	1.07 ± 0.10	0.17 ± 0.02	0.11 ± 0.01
Mn	0.11 ± 0.01	0.23 ± 0.05	0.19 ± 0.01
Fe	0.19 ± 0.02	1.26 ± 0.17	0.72 ± 0.08
Co	0.00 ± 0.01	0.00 ± 0.04	0.00 ± 0.15
Ni	0.00 ± 0.01	0.56 ± 0.16	0.18 ± 0.01
Cu	0.14 ± 0.01	0.04 ± 0.02	0.43 ± 0.06
Zn	3.30 ± 0.33	1.78 ± 0.27	1.10 ± 0.23

TRC105 conjugation, labeling, imaging, and biodistribution

A lower average ^{52}Mn-DOTA effective specific activity of 0.8 GBq/µmol compared to that of the typical ^{89}Zr-DFO assay (~30 GBq/µmol) motivated an increase in the bifunctional-chelate to antibody ratio (25:1) during conjugation. The resulting DOTA-TRC105 had excellent radiolabeling properties as shown in Table 3. 4 µg/MBq of DOTA-TRC105 was sufficient to reach ^{52}Mn complexation efficiencies greater than 95% after 60 minutes at 37 °C

Table 3: Radiolabeling efficiency of ^{52}Mn-DOTA-TRC105 as a function of antibody mass and time as measured by thin layer chromatography. Reactions took place at 37 °C in a pH 4.0-4.5 NaOAc buffered solution.

mAb mass (µg/MBq)	20 min	40 min	60 min
2.7	85%	89%	95%
6.8	98%	93%	99%
13.5	99%	95%	98%
27.0	99%	93%	100%

Injections of ^{52}Mn-DOTA-TRC105 were administered to Balb/c mice bearing 4T1 xenografts and PET data were collected. Maximum intensity projection (MIP) PET images are shown in Figure 2. ROI quantification of the ^{52}Mn-DOTA-TRC105 PET images yielded the time activity curves shown in Figure 3. Finally, the e*x vivo* biodistribution results shown in Figure 4 confirm the accuracy of image-based ROI quantification.

Tumor uptake peaked at the 24-hour PET time-point with an average value of 19 ± 3 %ID/g (n=3). The ^{52}Mn-DOTA-TRC105 time activity curves measured in this work agree well with those seen with ^{89}Zr-labeled TRC105 via desferrioxamine in the same animal and xenograft model[25] indicating a stable conjugate. Furthermore the increased DOTA conjugation ratio does not seem to perturb CD105 binding affinity. When comparing the ex vivo biodistribution of ^{89}Zr-DF-TRC105 to ^{52}Mn-DOTA-TRC105 the most significant difference is the slower blood clearance rate of ^{52}Mn-DOTA-TRC105 to ^{89}Zr-Df-TRC105. Assuming the same conjugate distribution, dosimetrically, ^{52}Mn is less favorable for injection compared to ^{89}Zr for immunoPET (see Supporting Information). However in some

instances the higher dose from ^{52}Mn may be justified for longer-term scanning, or its use in novel triple coincidence PET cameras.

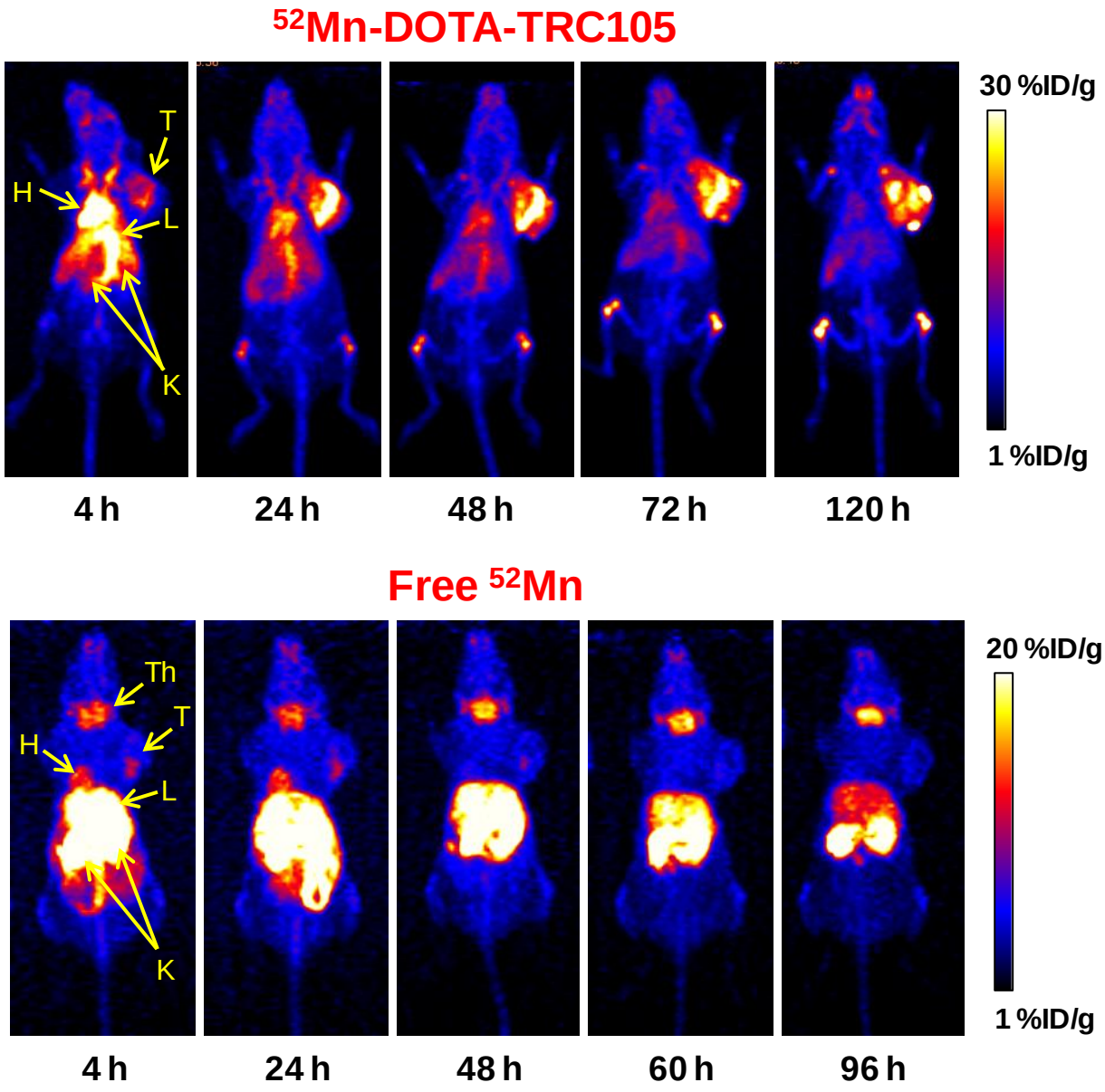

Figure 2: Serial maximum intensity projection (MIP) PET images of mice injected with ^{52}Mn-DOTA-TRC105 and $^{52}MnCl_2$. Significant thyroid accumulation in the $^{52}MnCl_2$ images contrasting the lack of uptake in the ^{52}Mn-DOTA-TRC105 images indicates highly stable DOTA chelation of $^{52}Mn^{2+}$ even at late time-points. Note – H: Heart, L: Liver, K: Kidneys, T: Tumor, Th: Thyroid.

Comparing ^{52}Mn-DOTA-TRC105 with the "Free ^{52}Mn"[2] PET images, there are clear differences in the distribution pattern. The most pronounced differences include a lack of thyroid uptake in the ^{52}Mn-DOTA-TRC105 images, and a lack of tumor

[2] No qualitative differences were observed between subjects injected with $^{52}MnCl_2$ (n=2) vs ^{52}Mn-Acetate (n=2), suggesting rapid ionic dissociation post-injection. These four subjects were therefore combined into a single "Free ^{52}Mn" group.

uptake in the $^{52}MnCl_2$ images. These features support that the DOTA chelation of ^{52}Mn is stable, even 120 hours post-injection. However, there is an enhanced signal in the bones with the targeted injections, but not in the free-ion case. Typically bone uptake in immunoPET is associated with instability of the metal-chelate pair. If this is the case in the present study, it is clear that the slow-dissociating manganese displays a pharmacokinetic profile that is distinct from the free manganese. One possible explanation is a direct interaction between the bone and the DOTA-bound manganese rather than a hydrolysis mechanism for chelate instability. Further investigation into the *in vivo* behavior of manganese salts may help determine the impact that slow dissociation has upon PET quantification, as has been done for ^{89}Zr.[29]

Impurities

Prior to translation there are many important considerations, especially concerning radionuclidic and chemical purity. The injections in this study contained approximately 0.5% radionuclidic impurity from ^{54}Mn, which contributes only in a small way to personal dosimetry (see Supporting Information), but the long half-life (biological and physical) may be an important factor in deciding whether or not to use enriched ^{52}Cr as an alternative target material: thereby eliminating production of ^{54}Mn. Chemically, the use of chromium in a pharmaceutical production may raise concerns of toxic effects. However, the amount of Cr that remains after purification is extremely low, at most 1µg for an entire production (150-250MBq). This Cr has no propensity to form a stable complex with functionalized DOTA[30] and would be further removed during the size-exclusion purification step. For comparison, the EPA reference dose, RfD, for Cr(IV), below which no effects are observed is 3µg/kg in rats[31]: a level much higher than would be reached following injection of a purified ^{52}Mn-immunoconjugate.

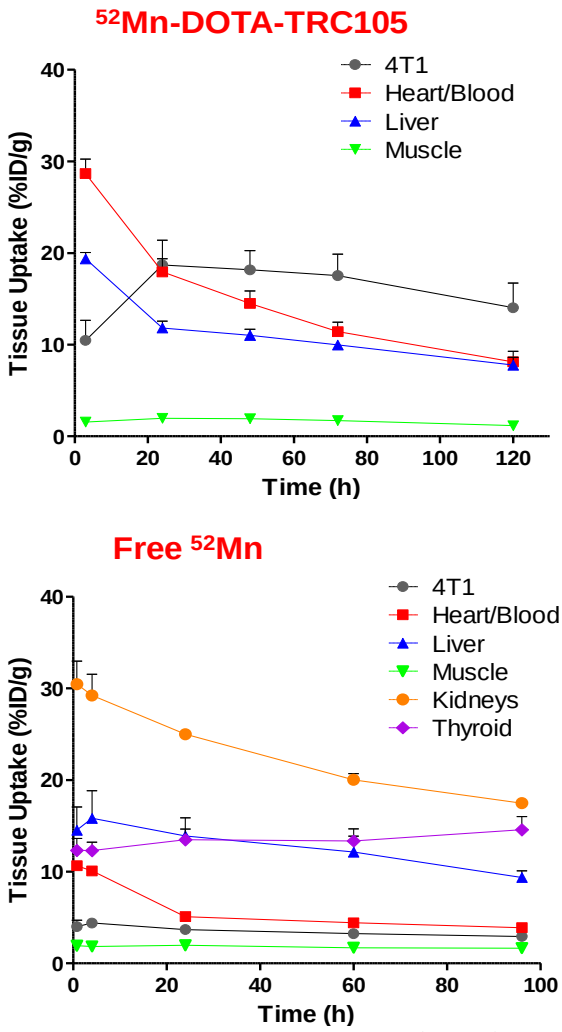

Figure 3: Time activity curves (TACs) acquired from ROI analysis of PET images obtained in subjects injected with ^{52}Mn-DOTA-TRC105 (n = 3) and with Free ^{52}Mn (n = 4). Error bars represent the standard deviation, and are displayed one-sided for visual clarity. The Heart/Blood TAC uses an ROI drawn over the left ventricle and does not differentiate myocardium from the blood pool.

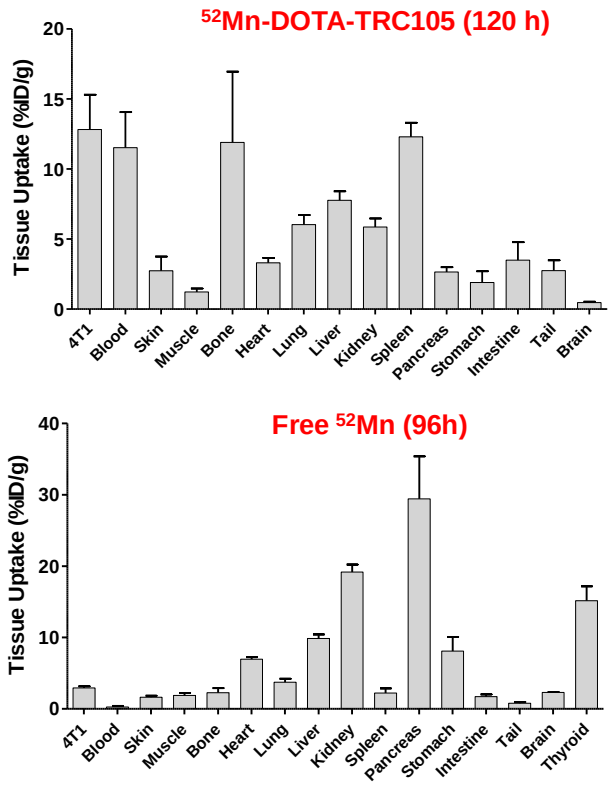

Figure 4: *Ex vivo* ^{52}Mn-DOTA-TRC105 (n = 3) and $^{52}MnCl_2$/^{52}Mn-acetate (n = 4) biodistribution data obtained following the last PET time point. Animals were sacrificed, and tissue samples were isolated, washed with saline, dried, weighed, and gamma counted.

Conclusion

The results above and methodology below are intended to provide an easily reproducible path towards investigating bioconjugate systems using ^{52}Mn. The example of ^{52}Mn-DOTA-TRC105 shows that stable chelation of manganese via bifunctionalized DOTA is suitable for tracing macromolecules with PET over the course of several days, with imaging characteristics that compare favorably to ^{89}Zr. Additionally, the effective specific activity of ^{52}Mn that results from anion-exchange separations from ethanol-HCl mixtures is sufficient to conduct antibody imaging.

Experimental Procedures

Materials

All reagents were obtained from commercial vendors and were used as received unless otherwise stated. TRC105 (mAb) was provided by TRACON Pharmaceuticals Inc. 4T1 murine breast cancer cells were obtained from the American Type Culture Collection (ATCC). Aqueous solutions were constituted in >18 MΩ/cm water. Unless noted, the term HCl refers to 32-35% aqueous hydrochloric acid Ethanol-HCl mixtures were made in v:v proportion using ethanol (molecular biology grade, Sigma Aldrich) and 32-35% aqueous HCl (untitrated, Optima grade, VWR).

Target Fabrication, Irradiation, Dissolution and Column Separation

Targets were constructed by placing a natural chromium pellet (99.999% pure, approximately 750 mg, GFS Chemicals) on the center of a 19 mm diameter 2 mm thick silver disc (>99.9% pure, Noble Metals, Sarasota, FL) before being folded between niobium foil and hydraulically pressed with a force of approximately 30 kN for ten seconds. This force was sufficient to imbed the chromium metal into the silver disc without compromising the integrity of the rear target face. These targets were irradiated by 16 MeV protons (GE PETtrace) with beam currents up to 60 µA.

Following irradiation, targets were etched by 2 mL of HCl (32-35%, Optima, VWR) at 75 °C for one hour, or until cessation of bubbling (typically 400 mg of the 750 mg Cr target was dissolved by this procedure). The solution was quantitatively transferred to a large centrifuge tube using a 47.5 mL rinse of ethanol (molecular biology grade, Sigma-Aldrich). To this solution, 0.5 mL of HCl was added resulting in a final target solution of 50 mL.

Three columns were constructed, each containing approximately 250 mg of dry AG-1x8 strong anion exchange resin (Bio-Rad Laboratories) and were equilibrated and rinsed with 10 mL of 97:3 ethanol-HCl. The 50 mL of target solution was passed through the first column trapping the ^{52}Mn and letting the bulk ^{nat}Cr pass through. After rinsing with 10 mL of 97:3 ethanol--HCl the activity was eluted in 1 mL of 6 M HCl. The eluted volume was diluted to 50 mL with ethanol, and then loaded on the second column. After rinsing, the activity was again eluted in 1 mL of 6M HCl and taken up to 50 mL with ethanol. With the activity loaded onto the third and final purification column, the column was rinsed, dried with air, and the activity was eluted in approximately 1 mL of 0.1 M of HCl. Due to mobile-phase retention in the resin, invariably the

final elution contained ethanol. It should be noted that for some labeling procedures, the eluted product should be dried down and reconstituted in 0.1M HCl or an appropriate buffer.

Trace Metal Analysis, and DOTA Chelation

An aliquot of ^{52}Mn from each production was taken to dryness under vacuum and reconstituted in a known volume of 0.1 M HCl. Trace concentrations of Cr, Mn, Fe, Co, Ni, Cu, and Zn were measured by microwave plasma atomic emission spectrometry (MP-AES, Agilent). Total metal impurity load for each production was calculated by dividing the sample masses by the fraction of the total activity used for this assay.

For chelation assays, 200 µl of ^{52}Mn activity in 0.1 M HCl was added to 600 µl of pH 4.5, 0.25 M NaOAc buffer. Vials containing 100 µl of increasing DOTA (Macrocyclics Inc.) concentrations were prepared ranging from 0 µg/ml to 10 µg/ml in water. A 100 µl aliquot of the buffered activity solution was added to each DOTA vial. Vials were vortexed, and left to complex at room temperature for one hour. Each sample was spotted on a thin layer chromatography (TLC) silica plate (60G F254, Merck KGaA) and was run with 0.25 M NH_4OH mobile phase. This method left unbound activity at the origin and moved ^{52}Mn-DOTA with the mobile phase. RadioTLC's were quantified by phosphor-storage plate autoradiography (Cyclone Plus, Perkin Elmer Inc.).

Preparation of the "Free $^{52}Mn^{2+}$" injections

Eluted ^{52}Mn fractions were taken to dryness under reduced atmosphere at 70 °C to remove acidity and EtOH contamination. $^{52}MnCl_2$ injections were prepared by reconstituting the dried ^{52}Mn in phosphate-buffered saline and ^{52}Mn-Acetate injections were prepared by reconstituting the dried ^{52}Mn in pH 7.5 0.1 M NaOAc.

DOTA-TRC105 Conjugation and ^{52}Mn Labeling

A solution containing TRC105 was adjusted to pH 8.5-9.0 with 0.1 M Na_2CO_3. p-SCN-Bn-DOTA (Macrocyclics) previously dissolved in DMSO was added to this solution in a 25:1 (DOTA : TRC105) molar ratio. Following this addition, the pH was measured and adjusted to pH 8.5-9.0 with Na_2CO_3. The conjugation reaction was allowed two hours to complete at room temperature before DOTA-TRC105 was purified by size exclusion chromatography (PD-10, GE-Healthcare) using phosphate-buffered saline (PBS) mobile phase.

75-110 MBq of ^{52}Mn in ~200 µl 0.1 M HCl was added to 500 µl 0.1 M pH 4.5 NaOAc. To determine the appropriate quantity of DOTA-TRC105, labeling was initially tested with 2.7, 6.8, 13.5 and 27.0 µg/MBq. ^{52}Mn labeling with these samples was monitored by radio-TLC using 50 mM pH 4.5 ethylenediamineetetraacetic acid (EDTA) mobile phase over the course of one hour at room temperature. TLC peak discrimination was used to distinguish between bound and unbound ^{52}Mn, and peak integration was used for quantification following a background subtraction.

For animal experiments, 4 µg of DOTA-TRC105 per MBq ^{52}Mn was added to the buffered activity solution and allowed to react for 60 minutes at 37 °C. After labeling, EDTA was added such that the resulting concentration was 1 mM. Labeling yield was quantified by radio-TLC, and the ^{52}Mn-DOTA-TRC105 was purified by size exclusion chromatography using PBS mobile phase. The resulting fraction was collected and passed through a 0.2 µm syringe filter prior to *in vivo* experiments.

Murine 4T1 Tumor Cell Line and Animal Model

4T1 cells were cultured in RPMI 1640 growth medium (Invitrogen) with 1x low serum growth supplement. During culturing, cells were incubated at 37 °C with 5% CO_2. Once cells reached approximately 75% confluence, they were used for *in vivo* experiments.

All animal studies were conducted under a protocol approved by the University of Wisconsin Institutional Animal Care and Use Committee. Tumors were established in four- to five-week-old female Balb/c mice purchased from Harlan Sprague Dawley Inc. by subcutaneous injection of approximately 2 x 10^6 cells, suspended in 100 µl of 1:1 mixture of RPMI 1640 and Matrigel (BD Biosciences), into the front flank of seven mice. Tumor sizes were monitored, and mice were used for imaging experiments when the diameter of tumors reached 5-8 mm (typically 1-2 weeks after inoculation).

Imaging and Biodistribution Studies

Mice were anesthetized with 2% isofluorane and 2.2 - 4.4 MBq of ^{52}Mn-DOTA-TRC105 (n=3), $^{52}MnCl_2$ (n=2), or ^{52}Mn-Acetate (n=2) was injected by tail vein in a rapid bolus. PET/CT imaging was

performed (Inveon microPET/CT, Siemens Inc.) at five time-points between 4 and 128 hours in the ^{52}Mn-DOTA-TRC105 group, and five time-points between 4 and 96 hours in the $^{52}Mn^{2+}$ control groups with at least 40 million coincident counts per PET acquisition. Static images were reconstructed using three-dimensional ordered subset expectation maximization (OSEM3D).

Following the last PET time-point, each animal was sacrificed. In addition to a blood draw, samples from the following tissues were extracted, washed in saline, and weighed: 4T1 tumor, skin, muscle, bone (femur, inferior half), heart, lung, liver, kidney, spleen, pancreas, stomach, intestine, tail, brain, and thyroid. ^{52}Mn activity in each sample was measured by gamma counting (Wizard 2480, PerkinElmer).

The results of both PET region of interest (ROI) and *ex vivo* biodistribution quantitative analysis were expressed as percent of the injected dose per gram of tissue (%ID/g ± SD).

Acknowledgements

We are grateful to Dr. Andreas Maurer at the University of Tübingen for sharing his experiences with DOTA-Mn reaction conditions. The authors acknowledge and are thankful for their funding from the University of Wisconsin - Madison, the DOE (DE-FG02-12ER41882), the National Science Foundation (DGE-1256259), the National Institutes of Health (5T32GM08349, 5 T32 CA009206-34, NIBIB/NCI 1R01CA169365, and P30CA014520), the American Cancer Society (125246-RSG-13-099-01-CCE), and the EU FP7 framework (MATHIAS).

Supporting Information

Dosimetry comparison between ^{89}Zr and ^{52}Mn, including contaminant ^{54}Mn[32-37]; tabulated ex vivo biodistribution data; Derenzo phantom images.

Competing Interests

Charles P. Theuer is an employee of TRACON Pharmaceuticals. The other authors have no competing interests to declare.

References

1. Deri, M. A., Zeglis, B. M., Francesconi, L. C., and Lewis, J. S. (2013) PET imaging with ^{89}Zr: From radiochemistry to the clinic, *Nucl. Med. Biol. 40*, 3-14.
2. Wadas, T. J., Wong, E. H., Weisman, G. R., and Anderson, C. J. (2010) Coordinating radiometals of copper, gallium, indium, yttrium, and zirconium for PET and SPECT imaging of disease, *Chem. Rev. 110*, 2858-2902.
3. Crossgrove, J., and Zheng, W. (2004) Manganese toxicity upon overexposure, *NMR Biomed. 17*, 544-553.
4. Pirko, I., Gamez, J., Shearier, E., Raman, M., Johnson, A., and Macura, S. (2012) Manganese Enhanced MRI (MEMRI) in Murine CNS Inflammatory Disease Models (S21. 007), *Neurology 78*, S21. 007.
5. Yamada, M., Momoshima, S., Masutani, Y., Fujiyoshi, K., Abe, O., Nakamura, M., Aoki, S., Tamaoki, N., and Okano, H. (2008) Diffusion-Tensor Neuronal Fiber Tractography and Manganese-enhanced MR Imaging of Primate Visual Pathway in the Common Marmoset: Preliminary Results, *Radiology 249*, 855-864.
6. Napieczynska, H., Calaminus, C., Severin, G. W., Fonslet, J., and Pichler, B. J. (2015) Mn-52 as a PET Neural Tract Tracer, In *European Molecular Imaging Meeting*, abstract # 301, March 19, 2015, Tuebingen, Germany.
7. Jacobs, K. E., Behera, D., Rosenberg, J., Gold, G., Moseley, M., Yeomans, D., and Biswal, S. (2012) Oral manganese as an MRI contrast agent for the detection of nociceptive activity, *NMR Biomed. 25*, 563-569.
8. Lin, Y. J., and Koretsky, A. P. (1997) Manganese ion enhances T1-weighted MRI during brain activation: An approach to direct imaging of brain function, *Magn. Reson. Med. 38*, 378-388.
9. Schima, W., Függer, R., Schober, E., Oettl, C., Wamser, P., Grabenwöger, F., Ryan, J. M., and Novacek, G. (2002) Diagnosis and Staging of Pancreatic Cancer: Comparison of Mangafodipir Trisodium—Enhanced MR Imaging and Contrast-Enhanced Helical

Hydro-CT, *Am. J. Roentgenol. 179*, 717-724.
10. Murakami, T., Baron, R. L., Peterson, M. S., Oliver 3rd, J., Davis, P. L., Confer, S. R., and Federle, M. P. (1996) Hepatocellular carcinoma: MR imaging with mangafodipir trisodium (Mn-DPDP), *Radiology 200*, 69-77.
11. Kim, T., Momin, E., Choi, J., Yuan, K., Zaidi, H., Kim, J., Park, M., Lee, N., McMahon, M. T., and Quinones-Hinojosa, A. (2011) Mesoporous silica-coated hollow manganese oxide nanoparticles as positive T 1 contrast agents for labeling and MRI tracking of adipose-derived mesenchymal stem cells, *J. Am. Chem. Soc. 133*, 2955-2961.
12. Gilad, A. A., Walczak, P., McMahon, M. T., Na, H. B., Lee, J. H., An, K., Hyeon, T., van Zijl, P., and Bulte, J. W. (2008) MR tracking of transplanted cells with "positive contrast" using manganese oxide nanoparticles, *Magn. Reson. Med. 60*, 1-7.
13. Hu, T. C. C., Pautler, R. G., MacGowan, G. A., and Koretsky, A. P. (2001) Manganese-enhanced MRI of mouse heart during changes in inotropy, *Magn. Reson. Med. 46*, 884-890.
14. Lang, C., Habs, D., Parodi, K., and Thirolf, P. (2014) Sub-millimeter nuclear medical imaging with high sensitivity in positron emission tomography using β+ γ coincidences, *J. Instrum. 9*, P01008.
15. Topping, G. J. (2014) Manganese imaging with positron emission tomography, autoradiography, and magnetic resonance, PhD Thesis, University of British Columbia, Vancouver, Canada, February 2014.
16. Wooten, A. L., Lewis, B. C., and Lapi, S. E. (2015) Cross-sections for (p, x) reactions on natural chromium for the production of ^{52,} ^{52m,} ^{54}Mn radioisotopes, *Appl. Radiat. Isot. 96*, 154-161.
17. Topping, G. J., Schaffer, P., Hoehr, C., Ruth, T. J., and Sossi, V. (2013) Manganese-52 positron emission tomography tracer characterization and initial results in phantoms and in vivo, *Med. Phys. 40*, 042502.
18. Buchholz, M., Spahn, I., Scholten, B., and Coenen, H. H. (2013) Cross-section measurements for the formation of manganese-52 and its isolation with a non-hazardous eluent, *Radiochim. Acta 101*, 491-499.
19. Lewis, C. M., Graves, S. A., Hernandez, R., Valdovinos, H. F., Barnhart, T. E., Cai, W., Meyerand, M. E., Nickles, R. J., and Suzuki, M. (2015) ^{52}Mn production for PET/MRI tracking of human stem cells expressing divalent metal transporter 1 (DMT1), *Theranostics 5*, 227.
20. Daube, M., and Nickles, R. (1985) Development of myocardial perfusion tracers for positron emission tomography, *Int. J.Nucl.Med. Biol. 12*, 303-314.
21. Pietrzyk, D. J. (1960) Anion Exchange Separations of Metal Ions in Partially Nonaqueous Solutions, *Retrospective Theses and Dissertations Paper 2390*, Iowa State University.
22. Bianchi, A., Calabi, L., Giorgi, C., Losi, P., Mariani, P., Palano, D., Paoli, P., Rossi, P., and Valtancoli, B. (2001) Thermodynamic and structural aspects of manganese (II) complexes with polyaminopolycarboxylic ligands based upon 1, 4, 7, 10-tetraazacyclododecane (cyclen). Crystal structure of dimeric [MnL] 2· 2CH 3 OH containing the new ligand 1, 4, 7, 10-tetraazacyclododecane-1, 4-diacetate, *J. Chem. Soc., Dalton Trans.*, 917-922.
23. Junde, H., Su, H., and Chunhui, M. (2007) Nuclear data sheets for A= 52, *Nucl. Data Sheets 108, 773-882.*
24. Engle, J. W., Hong, H., Zhang, Y., Valdovinos, H. F., Myklejord, D. V., Barnhart, T. E., Theuer, C. P., Nickles, R. J., and Cai, W. (2012) Positron emission tomography imaging of tumor angiogenesis with a ^{66}Ga-labeled monoclonal antibody, *Mol. Pharmaceutics 9*, 1441-1448.
25. Hong, H., Severin, G. W., Yang, Y., Engle, J. W., Zhang, Y., Barnhart, T. E., Liu, G., Leigh, B. R., Nickles, R. J., and Cai, W. (2012) Positron emission tomography imaging of CD105 expression with ^{89}Zr-Df-TRC105, *Eur. J. Nucl. Med. Mol. Imaging 39*, 138-148.
26. Zhang, Y., Hong, H., Engle, J. W., Bean, J., Yang, Y., Leigh, B. R., Barnhart, T. E., and Cai, W. (2011) Positron Emission

Tomography Imaging of CD105 Expression with a ^{64}Cu-Labeled Monoclonal Antibody: NOTA Is Superior to DOTA, *PLoS ONE 6*, e28005.

27. Venkatraman, M., and Neumann, J. P. (1990) The Ag-Cr (Silver-Chromium) system, *Bull. of Alloy Phase Diagrams 11*, 263-265.
28. Knox, K. (1990) Fast and slow reactions of chromium compounds, *J. Chem. Educ. 67*, 700.
29. Severin, G. W., Jorgensen, J. T., Wiehr, S., Rolle, A. M., Hansen, A. E., Maurer, A., Hasenberg, M., Pichler, B., Kjaer, A., and Jensen, A. I. (2015) The impact of weakly bound ^{89}Zr on preclinical studies: non-specific accumulation in solid tumors and aspergillus infection, *Nucl. Med. Biol. 42*, 360-368.
30. Asti, M., Tegoni, M., Farioli, D., Iori, M., Guidotti, C., Cutler, C. S., Mayer, P., Versari, A., and Salvo, D. (2012) Influence of cations on the complexation yield of DOTATATE with yttrium and lutetium: a perspective study for enhancing the ^{90}Y and ^{177}Lu labeling conditions, *Nucl. Med.Biol. 39*, 509-517.
31. Agency, U. S. E. P. (1999) Integrated Risk Information System (IRIS) on Chromium VI., In *National Center for Environmental Assessment, Office of Research and Development, Washington, D. C.*
32. Ishinishi, N., and Morishige, T. (1969) A Study on the Distribution of ^{95}Zr-^{95}Nb Administered Subcutaneously to Rats: Comparison between Young and Adult Rats, *J.Radiat.Res. 10*, 101-106.
33. O'Neal, S. L., Hong, L., Fu, S., Jiang, W., Jones, A., Nie, L. H., and Zheng, W. (2014) Manganese accumulation in bone following chronic exposure in rats: Steady-state concentration and half-life in bone, *Toxicol. Lett. 229*, 93-100.
34. Greiter, M. B., Giussani, A., Höllriegl, V., Li, W. B., and Oeh, U. (2011) Human biokinetic data and a new compartmental model of zirconium—A tracer study with enriched stable isotopes, *Sci. Total Environ. 409*, 3701-3710.
35. Mealey, J. (1957) Turn-over of carrier-free zirconium-89 in man, *Nature 179*, 673-674
36. Mahoney, J. P., and Small, W. J. (1968) Studies on manganese: III. The biological half-life of radiomanganese in man and factors which affect this half-life, *J. Clin. Invest. 47*, 643.
37. Stabin, M. G., Sparks, R. B., and Crowe, E. (2005) OLINDA/EXM: the second-generation personal computer software for internal dose assessment in nuclear medicine, *J. Nucl. Med. 46*, 1023-1027.

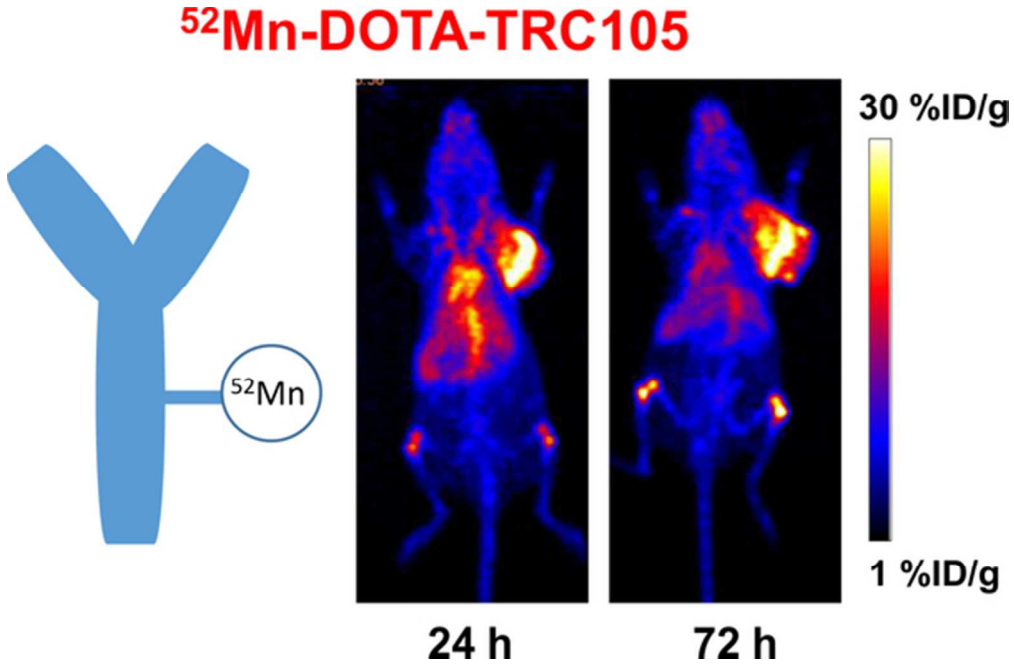

Table of Contents Graphic
50x33mm (300 x 300 DPI)

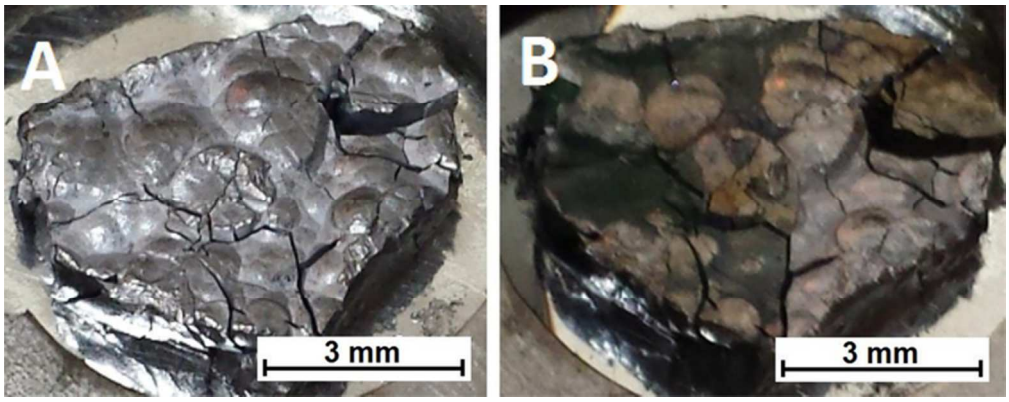

Figure 1: 99.999% pure chromium pellet embedded in silver, direct-jet watercooled on the rear target face, before (A) and after (B) irradiation by 60 μA of 16 MeV protons for one hour.
33x13mm (600 x 600 DPI)

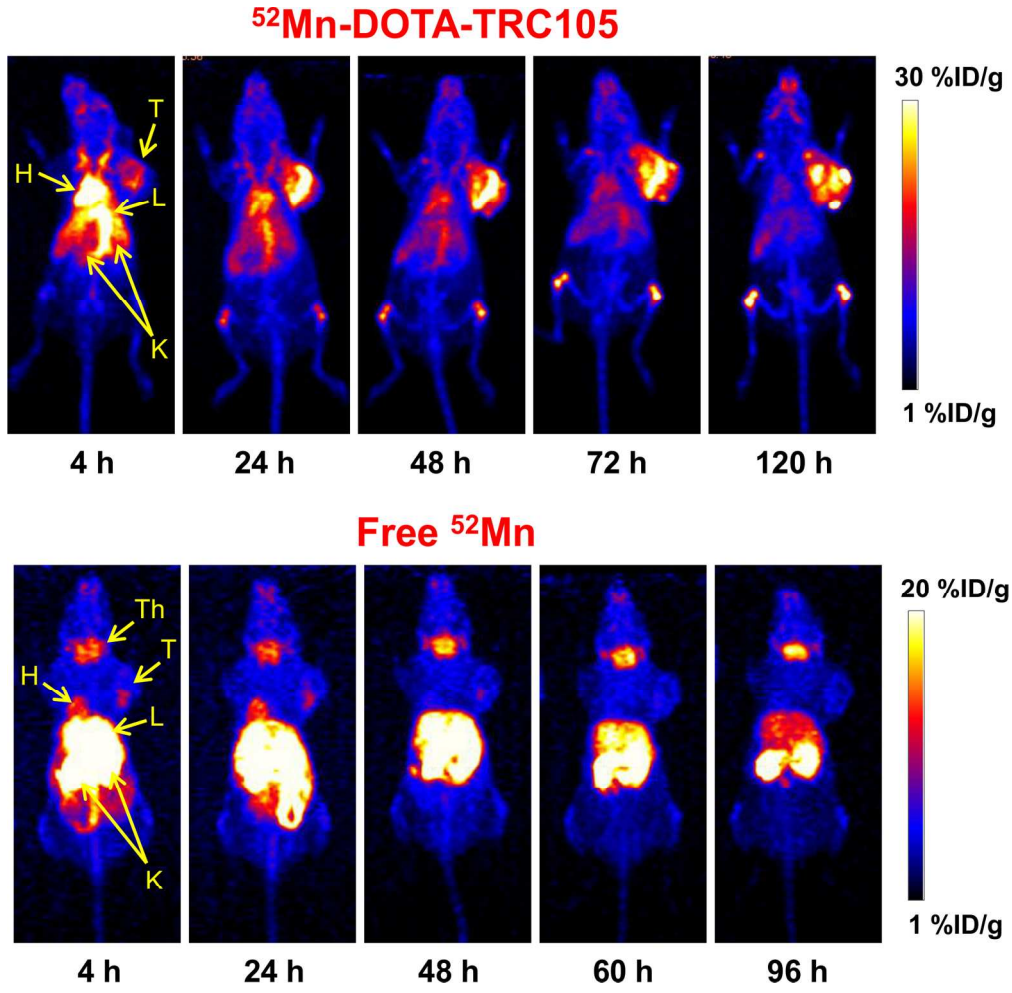

Figure 2: Serial maximum intensity projection (MIP) PET images of mice injected with ^{52}Mn-DOTA-TRC105 and $^{52}MnCl_2$. Significant thyroid accumulation in the $^{52}MnCl_2$images contrasting the lack of uptake in the ^{52}Mn-DOTA-TRC105 images indicates highly stable DOTA chelation of $^{52}Mn^{2+}$ even at late time-points. Note – H: Heart, L: Liver, K: Kidneys, T: Tumor, Th: Thyroid.
161x157mm (300 x 300 DPI)

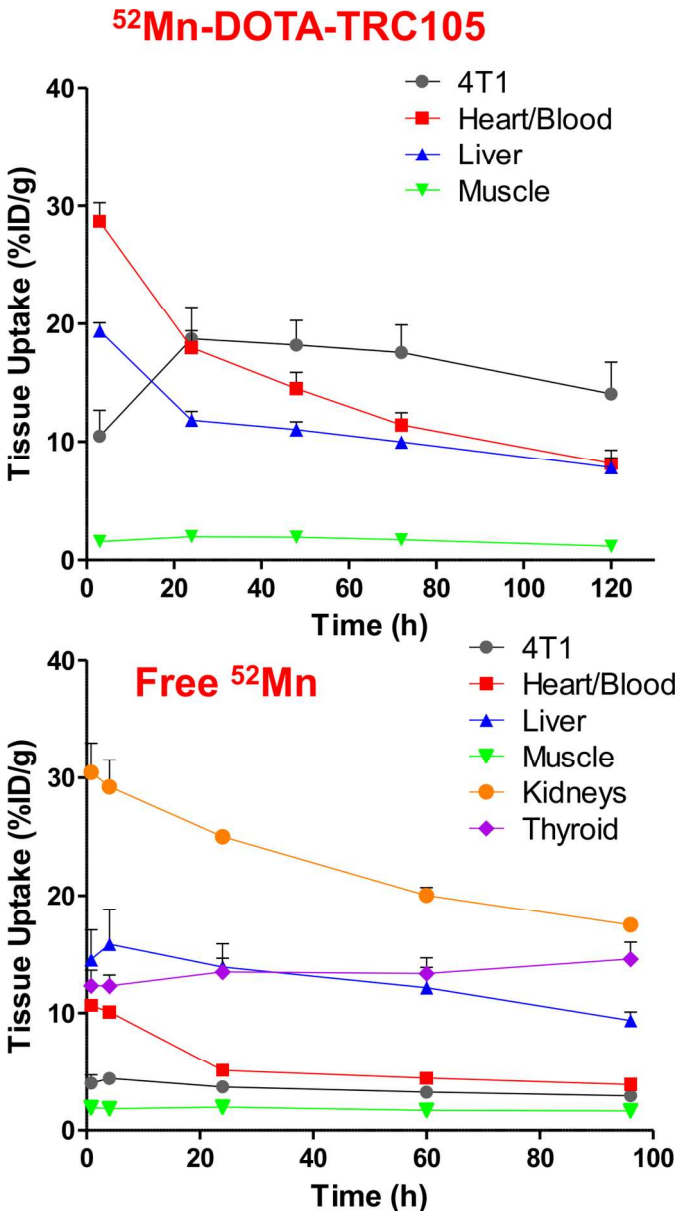

Figure 3: Time activity curves (TACs) acquired from ROI analysis of PET images obtained in subjects injected with ^{52}Mn-DOTA-TRC105 (n = 3) and with Free ^{52}Mn (n = 4). Error bars represent the standard deviation, and are displayed one-sided for visual clarity. The Heart/Blood TAC uses an ROI drawn over the left ventricle and does not differentiate myocardium from the blood pool.
153x276mm (300 x 300 DPI)

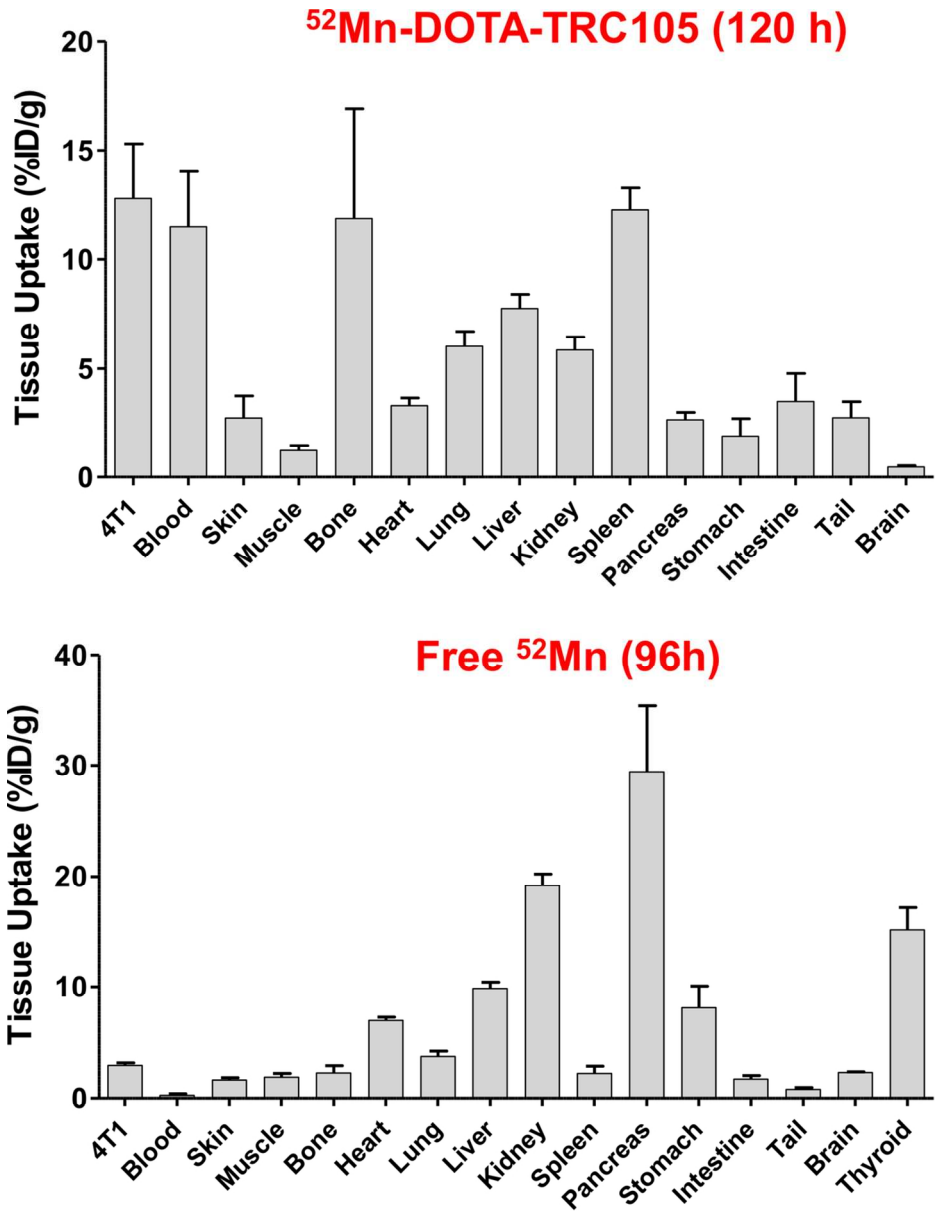

Figure 4: Ex vivo ^{52}Mn-DOTA-TRC105 (n = 3) and $^{52}MnCl_2$/^{52}Mn-acetate (n = 4) biodistribution data obtained following the last PET time point. Animals were sacrificed, and tissue samples were isolated, washed with saline, dried, weighed, and gamma counted.
110x142mm (300 x 300 DPI)